

## THE INTERACTION BETWEEN CYLINDERS AND NON-BOUSSINESQ GRAVITY CURRENTS

**Peter Brearley**

Department of Aeronautics  
 Imperial College London  
 London, United Kingdom  
 p.brearley@imperial.ac.uk

**Paul Bartholomew**

EPCC  
 University of Edinburgh  
 Edinburgh, United Kingdom  
 p.bartholomew@epcc.ed.ac.uk

**Sylvain Laizet**

Department of Aeronautics  
 Imperial College London  
 London, United Kingdom  
 s.laizet@imperial.ac.uk

### ABSTRACT

Three-dimensional non-Boussinesq gravity currents propagating into a horizontal circular cylinder in a lock-exchange configuration have been simulated using implicit large-eddy simulations. The findings show that the normalised drag force remains consistent across different density ratios when the object is close to the ground, but reduces for large density ratios as the distance from the ground increases. The variation in the drag and lift forces in the spanwise direction increases substantially with widening density ratios, resulting in non-uniform, oscillatory loading and strong local forces that are not predicted by the overall force calculation. This is an important consideration for structure design in gravity current-prone regions.

### INTRODUCTION

Gravity currents are fluid flows driven by density differences, causing the denser fluid to propagate across a surface under the less dense fluid. These currents are the means of a range of oceanic, atmospheric and geological flows that play a crucial role in regulating Earth's climate by redistributing heat around the planet. In the ocean, gravity currents include the vast deep-sea currents shaped through differences in temperature and salinity and the turbidity currents generated by sediment movement along the ocean floor from sub-sea landslides. Atmospheric gravity currents can manifest as cold fronts, where dense, cold air displaces warm, light air at the Earth's surface. On land, dust storms, avalanches and pyroclastic flows are examples of gravity currents arising from sediment transport.

The density ratio between the current and the ambient fluid can range from fractions of a percent to several multiples depending on the application. In the ocean, differences in temperature lead to small density ratios that can drive huge volumes of seawater around the planet. The Navier-Stokes equations under the Boussinesq approximation consider the fluid to be incompressible aside from the buoyancy term in the momentum equations, and are commonly used for simulating density-stratified flows. However, it is only valid for small variations in density, typically less than 2%, which is restrictive for many applications such as atmospheric flows, turbidity currents, and pyroclastic flows.

When interacting with physical objects such as geological formations, submarine structures or city landscapes, gravity currents can exhibit complex behaviours. A two-way interaction occurs where the object disrupts the flow while the flow

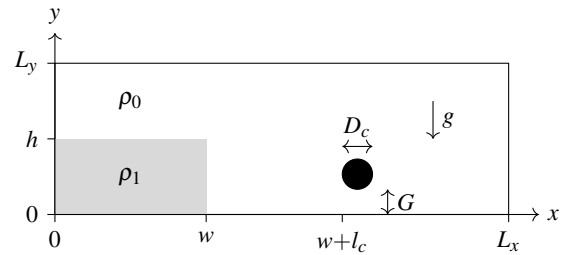


Figure 1. The lock-exchange configuration (not to scale)

exerts considerable force on the object. This interaction is of particular importance when considering the durability of man-made objects, such as the offshore structures and pipelines in the oil and gas and telecommunications industries, particularly as deeper ocean environments are being explored that are more vulnerable to high-velocity gravity currents.

Research into gravity currents has been conducted in a variety of configurations, including propagating across inclined surfaces (Albert, 2014), interacting with sudden slopes and overhangs (Maggi *et al.*, 2023), past staggered arrays of objects representing surface roughness (Ozan *et al.*, 2015), and interacting with a variety of objects, e.g. bottom-mounted square cylinders (Ermanyuk & Gavrilov, 2005b; Gonzalez-Juez & Meiburg, 2009; Gonzalez-Juez *et al.*, 2009; Zhou & Venayagamoorthy, 2017), bottom-mounted triangular cylinders (Tokuyay & Constantinescu, 2015), horizontal circular cylinders (Ermanyuk & Gavrilov, 2005a; Gonzalez-Juez *et al.*, 2010; Wang & Yoon, 2015; Xie *et al.*, 2022) and vertical circular cylinders (Brito *et al.*, 2022). The aforementioned studies are either experimental (Ermanyuk & Gavrilov, 2005a,b; Albert, 2014; Maggi *et al.*, 2023) or use large-eddy simulations (LES) of an incompressible fluid using the Boussinesq approximation. The interactions between non-Boussinesq gravity currents and physical objects are yet to be studied numerically, and are investigated here using implicit large-eddy simulations (ILES)

Details of the lock-exchange configuration and numerical methodology are provided in the next section, followed by the results and a discussion of the findings. The conclusions follow in the final section.

### IMPLEMENTATION

The lock-exchange configuration shown in Fig. 1 is used as it provides a consistent method of varying the parameters

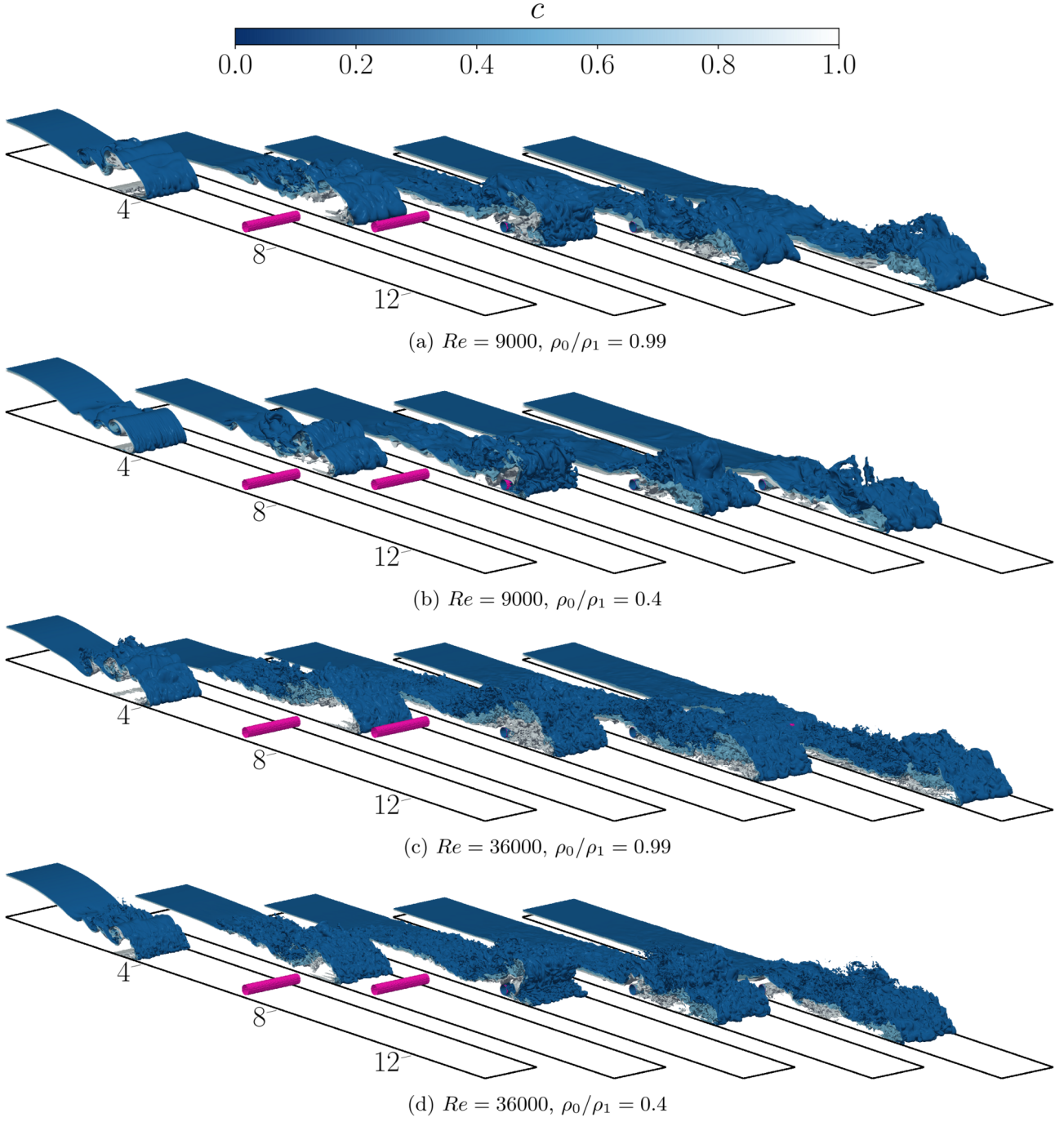


Figure 2. Evolution of the density isosurfaces  $c = 0.2$  (light grey),  $0.5$  (pale blue) and  $0.8$  (dark blue) at nondimensional time  $t/T_b = 4, 8, 12, 16, 20$  (left to right). Reynolds number varies as  $Re = 9000$  and  $36000$  and the density ratio varies as  $\rho_0/\rho_1 = 0.99$  and  $0.4$ . The cylinder height is kept constant at  $G/h = 0.05$ . The surface of the cylinder is shown in pink. The axis displays the  $x/h$  values.

of the study. The heavier fluid with density  $\rho_1$  is filled to a height  $h$  in a tank of length  $L_x/h = 14.2$ , height  $L_y/h = 2.5$  and width  $L_z/h = 1.25$ , separated from the ambient fluid by a gate located at  $w/h = 2$ . A horizontal circular cylinder of diameter  $D_c/h = 0.2$  is located downstream of the current at a distance of  $l_c/h = 5$  from the dense fluid. Parameters to study are the density ratio  $\rho_0/\rho_1 = [0.99, 0.8, 0.6, 0.4]$ , the gap between the cylinder and the ground  $G/h = [0.05, 0.2]$ , and the Reynolds number  $Re = U_b h/\nu = [9000, 36000]$ , leading to 16 cases. The buoyancy velocity scale is defined as  $U_b = \sqrt{g'h}$ , where  $g' = g(\rho_1 - \rho_0)/\rho_0$  is the reduced gravity,  $g$  is the acceleration due to gravity and  $\nu$  is the kinematic viscosity. The buoyancy velocity and initial fill height can be used to

define a nondimensional buoyancy time scale  $T_b = h/U_b$ . The gate is removed at  $t = 0$  and the subsequent propagation of the dense fluid and its interaction with the cylinder is simulated.

To achieve this numerically, the open-source code Xcompact3D is used to solve the non-dimensional incompressible variable-density Navier-Stokes equations (Bartholomew & Laizet, 2019; Bartholomew *et al.*, 2020). Following the methodology of Birman *et al.* (2005) and Espath *et al.* (2014, 2015), the fluid density  $\rho = (\rho_1 - \rho_0)c + \rho_0$  is linearly related to the concentration of a species, where  $\rho_0$  is the density of the ambient light fluid,  $\rho_1$  is the initial density of the heavier fluid and  $c$  is the species concentration. Since the density varies linearly with  $c$ , a diffusion term is added to the continu-

ity equation

$$\frac{\partial \rho}{\partial t} + \frac{\partial(\rho u_k)}{\partial x_k} = \frac{1}{ReSc} \frac{\partial^2 \rho}{\partial x_k \partial x_k} \quad (1)$$

where  $Sc = \nu/D$  is the Schmidt number and  $D$  is the mass diffusivity. Equation (1) and the momentum equation are solved using a sixth-order compact finite difference scheme for the spatial derivatives and a second-order Adams-Bashforth scheme for time integration. A fractional-step strategy is employed where initially only the advection, viscous stress and buoyancy terms of the momentum equation are evaluated to produce an estimate of the velocity at the next time step. A Poisson equation is formed to evaluate the pressure and is solved in spectral space using a constant-coefficient solver, which is typically valid for density ratios of up to five (Bartholomew & Laizet, 2019). Full details of the numerical methods can be found in Laizet & Lamballais (2009) and Bartholomew & Laizet (2019). The cylinder is represented on the Cartesian mesh using a standard immersed boundary method (IBM), which is used to enforce a velocity and species concentration of zero in the cylinder region. This cylinder implementation was used successfully by Gonzalez-Juez *et al.* (2010) in their study of Boussinesq gravity currents.

The computational domain of size  $(L_x L_y L_z)/h = 14.2 \times 2.5 \times 1.25$  is discretised using a Cartesian mesh of  $N_x N_y N_z = 2001 \times 321 \times 100$  grid points that is stretched in the  $y$ -direction, ensuring  $D_c/\Delta y = 100$  and  $D_c/\Delta x = 28$  grid points within the cylinder. The  $y = 0$  boundary is specified as a no-slip wall and the  $y = L_y$ ,  $x = 0$  and  $x = L_x$  boundaries are specified as free-slip walls. The computational domain is periodic in the  $z$  direction.

The ILES are performed using a spectral vanishing viscosity (SVV) approach (Frantz *et al.*, 2021), which introduces numerical dissipation targeted at the small scales through the second derivative operators for the viscous terms in the Navier-Stokes equations. The SVV method is similar to the hyperviscosity model (Haugen & Brandenburg, 2004) but the dissipation can be targeted at high wavenumbers, making it well-suited to ILES. The ratio between the SVV at  $\kappa = 2/3\kappa_c$  and  $\kappa = \kappa_c$  that controls the active wavenumbers is set to 0.22, where the mesh cut-off wavenumber  $\kappa_c = \pi/\Delta x$ . The ratio between the SVV and the background viscosity,  $\nu_0/\nu = 10$  for the  $Re = 9000$  cases and  $\nu_0/\nu = 100$  for the  $Re = 36000$ , is based on the data from Frantz *et al.* (2021), who also demonstrated a general insensitivity of the model to variations in  $\nu_0/\nu$  of the correct order of magnitude. The SVV method has been successfully used in a gravity current configuration and compared against the dynamic and standard Smagorinsky models, and accurately reproduced the results at a much lower computational cost (Frantz *et al.*, 2021). The simulations have been validated by comparing against the standard Smagorinsky model in explicit LES as well as in a grid independence study using  $3001 \times 500 \times 200$  mesh nodes, where it was found that the current front location and the force evolution on the cylinder were in very close agreement.

## RESULTS AND DISCUSSION

The evolution of the density isosurfaces for some selected cases is shown in Fig. 2. The figure shows that the large region of fluid with density  $\rho_1$  is retained up to the interaction with the cylinder, which causes mixing with the ambient fluid in the cylinder wake. The front propagation velocity remains

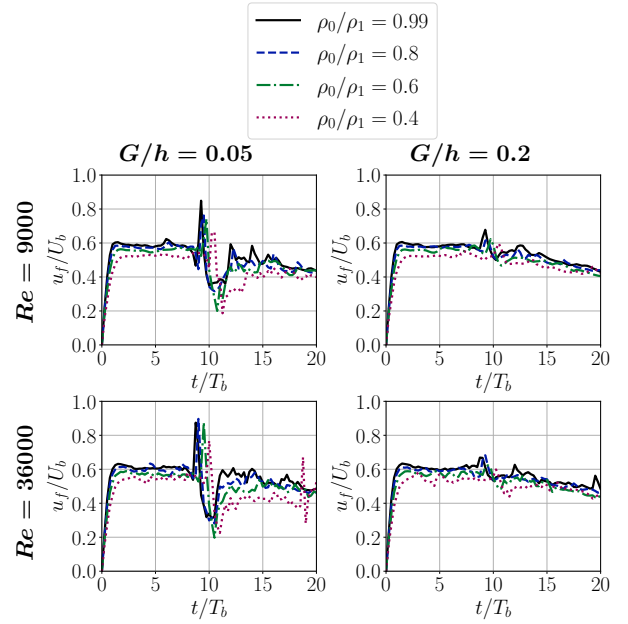


Figure 3. The gravity current propagation speed normalised by the buoyancy velocity, calculated as the velocity of the frontmost  $c = 0.1$  contour.

mostly proportional to the buoyancy velocity  $U_b$  in all cases, although the  $\rho_0/\rho_1 = 0.4$  is visibly propagating at a slower pace in nondimensional time.

The front velocity, defined as the velocity of the frontmost  $c = 0.1$  contour, is plotted in Fig. 3 for all cases, which shows the reduction in the dimensionless propagation speed with widening density ratio. The front-propagation velocity scale  $U_f$  can be defined by averaging  $u_f$  in the steady-state region prior to the cylinder interaction in the  $t/T_b = 2.5$  to  $7.5$  region. The values are shown in Table 1, which show the reduction in dimensionless propagation speed with  $\rho_0/\rho_1$  and the increase in dimensionless propagation speed with  $Re$ . These findings are consistent with the experimental data of Shin *et al.* (2004), who reported speeds of  $U_f/U_b = 0.57$  and  $0.60$  for  $L_y/h = 2$  and  $3$  respectively for Boussinesq currents. For the  $L_y/h = 2.5$  value used here,  $U_f/U_b$  lies between these values for the low  $Re$  case, showing good agreement. For the  $G/h = 0.05$  case, there is a sharp rise in  $u_f$  during the impact with the cylinder. This is caused by the narrow gap between the cylinder and the wall that accelerates the fluid, forming a high-velocity jet that later rejoins with the rest of the current downstream of the cylinder.

Table 1. Front propagation speeds

$\rho_0/\rho_1$	$U_f/U_b$ ( $Re=9k$ )	$U_f/U_b$ ( $Re=36k$ )
0.99	0.589	0.609
0.8	0.576	0.596
0.6	0.557	0.571
0.4	0.525	0.545

The front velocity scale  $U_f$  can be used to define a front propagation time scale  $T_f = h/U_f = T_b U_b/U_f$ , that allows a more ready comparison of the currents as they propagate. The

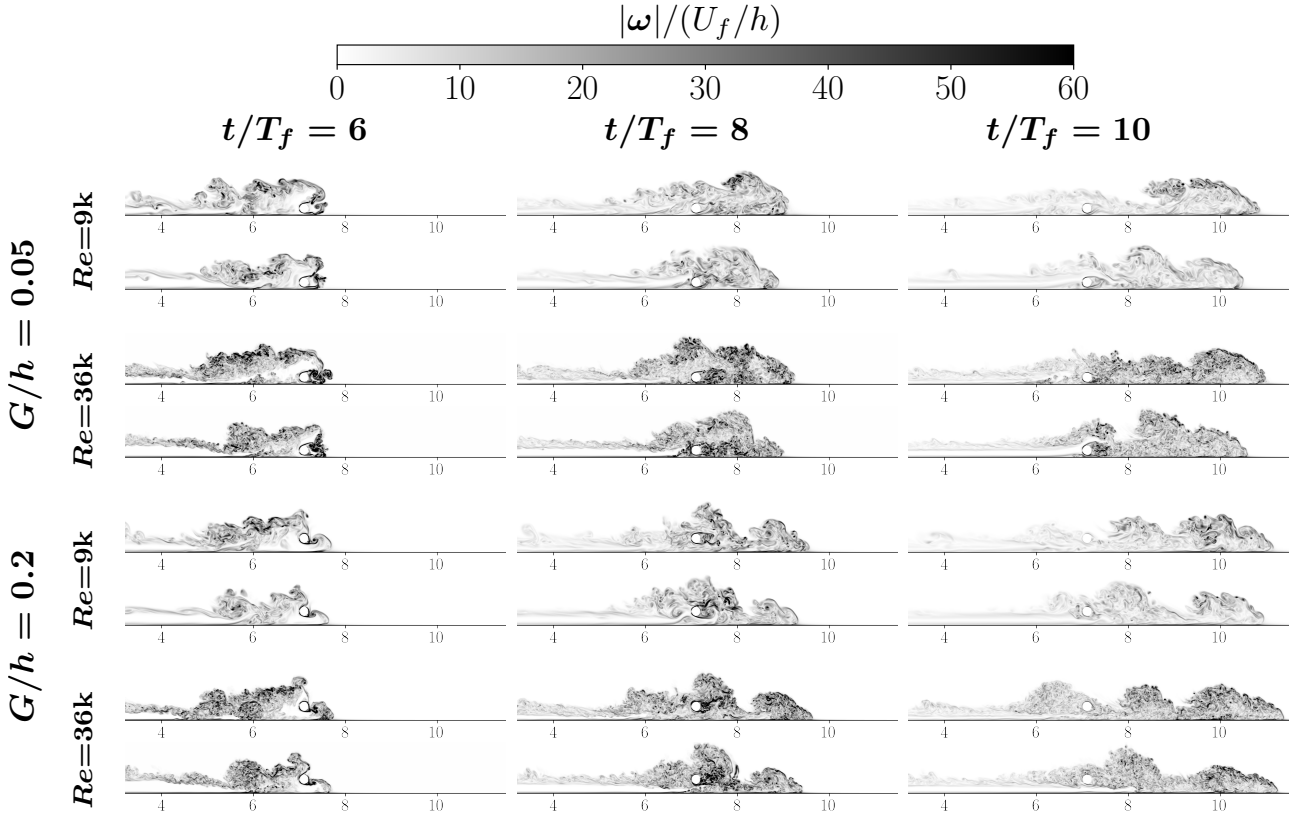


Figure 4. Contours of the normalised vorticity vector magnitude for the  $\rho_0/\rho_1 = 0.99$  cases (first row) and the  $\rho_0/\rho_1 = 0.4$  cases (second row). The axis displays the  $x/h$  value.

dimensionless vorticity magnitude is shown for different values of  $t/T_f$  in Fig. 4. The figure shows the jet of fluid that passes underneath the cylinder in both cases, more visible for the higher cylinder case but at a higher velocity for the lowest cylinder cases. The flow separation immediately in the wake of the cylinder entrains ambient fluid into the wake that mixes intensely with the denser fluid. The wake of the cylinder sees an increase in the vorticity and this is particularly pronounced for the  $Re = 36000$  cases. The relatively denser gravity currents see a reduced vorticity at the interface of the light and heavy fluids in all cases, and appear to cause a stronger normalised vorticity magnitude immediately in the cylinder wake.

The evolution of the spanwise-averaged force exerted on the cylinder is shown in Fig. 5. The forces are normalised by  $(0.5\rho_m DU_f^2)$ , where  $\rho_m = (\rho_0 + \rho_1)/2$  is the midpoint of the heavy and the light fluid densities. Figure 5 is therefore related to the force coefficients, although the normalisation factor is constant and does not account for the locally changing density and decaying front velocity. The normalised drag force, shown in Fig. 5a, peaks at consistent values for the lowest cylinder cases at different density ratios, while the highest cylinder cases see a substantial reduction in the normalised drag force as the density ratio widens. This is due to the denser fluid accumulating closer to the ground for the large density ratios, thus having a stronger interaction with the cylinder. Increasing the Reynolds number also appears to increase the impact drag force, particularly in the lowest cylinder case due to a thinner boundary layer. The spanwise-averaged lift force (shown in Fig. 5b) remains almost entirely positive for the lowest cylinder cases, as the denser fluid passing underneath at high velocity exerts a large upward force on the cylinder. On the other hand, for the higher cylinder cases, the lift force initially oscillates due to vortex-shedding effects, before taking

on a positive value in the steady stage. A widening density ratio causes more oscillatory lift forces and this can be seen in all cases. The total spanwise-averaged force is shown in Fig. 5, where total force is evaluated from the drag and lift forces as  $F = \sqrt{F_D^2 + F_L^2}$ . This reveals that the higher cylinder case causes stronger overall forces in the impact stage due to the strong vertical forces from the vortex shedding. In the steady stage, the overall forces are greater for the lowest cylinder case once the vortex shedding decays but the large upward forces due to the dense fluid passing underneath the cylinder remain. The total force shows a decrease with a widening density ratio for the high cylinder case due to the reduction in drag forces as the densest fluid can pass underneath the cylinder, exerting minimal force. The total force shows a consistent increase with  $Re$  across all cases, which primarily arises from an increase in drag.

The spanwise variation of the total force is shown in Fig. 6 for  $t/T_f = 8$ , which immediately reveals that a widening density ratio leads to a much greater variation in the force exerted on an object. This is especially the case for the low cylinder height cases. An increase in Reynolds number also brings about sharper and more frequent spikes in the force. These effects are masked when just considering the average force exerted but are an important design consideration due to large maximum forces, bending moments and cyclic loading.

The variation over time can be visualised by plotting the standard deviation of the force fluctuations about the spanwise-averaged mean,  $\sigma_F = \sqrt{F'^2}$  where  $F' = \bar{F} - F$  is the fluctuating component of the force. The standard deviation for the drag and lift components of the force are shown in Fig. 7, revealing that the source of the variation occurs in both components. The lowest cylinder height cases have the

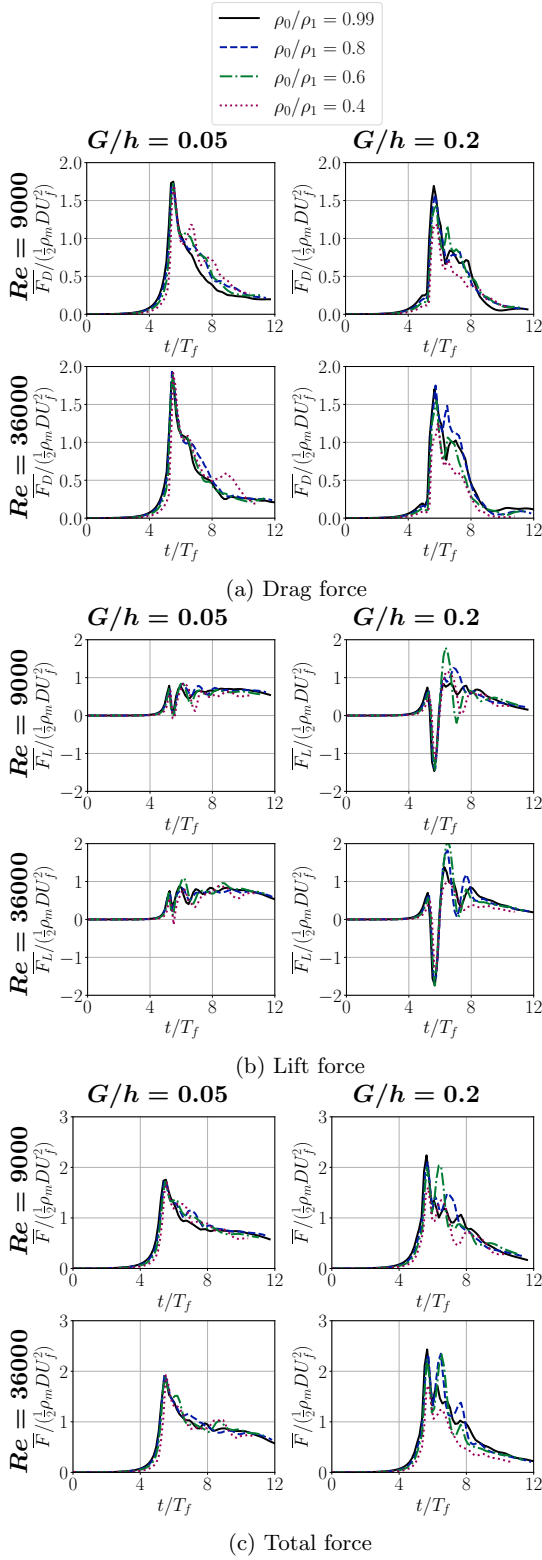


Figure 5. The spanwise-averaged drag force  $\overline{F}_D$ , lift force  $\overline{F}_L$  and total force  $\overline{F} = \sqrt{F_D^2 + F_L^2}$  per unit length of the cylinder.

greatest variability as the density ratio widens due to more interaction with the dense fluid. The standard deviation of the both the drag and lift forces are strongest in the impact stage, and this occurs due to the sharper and better-defined lobe and cleft structures of the dense gravity currents. The differences in the lobe and cleft structures can be visualised in Fig. 2 for the first two rows prior to the impact. The standard deviation

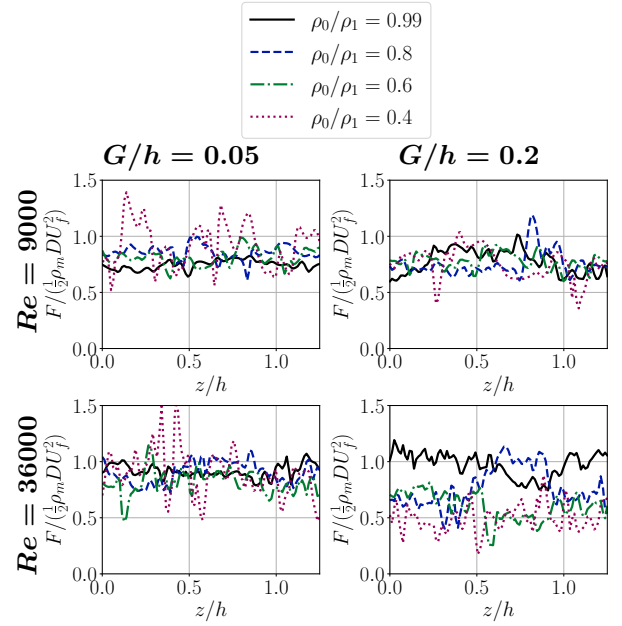


Figure 6. Spanwise variation of forces at  $t/T_f = 8$ .

itself also shows significant fluctuations, sharply dropping after the initial impact as the current loads the object more uniformly. The standard deviation of the forces continues to spike with a decaying magnitude in the lowest cylinder cases, as the turbulence induced towards the tail of the current interacts with the cylinder. As the cylinder height increases, the impact stage does not experience the greatest deviation, but the transient stage, and this deviation occurs more consistently across all cases. However, it can be seen from Fig. 5c that the total averaged normalised force is less for the dense gravity currents, so calculating the coefficient of variation by dividing the standard deviation by the mean does reveal greater fluctuations as a percentage of the mean. In the steady stage, the standard deviation of the force decays in all cases as the turbulence and current velocity decay over time, and as the local density approaches that of the ambient fluid due to mixing.

## CONCLUSIONS

The interactions between gravity currents and cylinders have been studied for a range of non-Boussinesq density ratios. The denser currents demonstrated similar overall force coefficients to Boussinesq currents when using the density midpoint for normalisation, but showed more force variation in the spanwise direction and over time. This non-uniform object loading is an important consideration for structure design due to high maximum forces, strong bending moments and material fatigue. The height of the cylinder has a significant effect on the forces exerted by currents with large density ratios; objects situated closer to the ground encountered higher drag forces and increased variability due to the accumulation of dense fluid in these regions. Further study into these effects is an important direction of future research. In particular, the effect of varying in the Schmidt number and the effects of particle suspension in the numerical models are important to investigate.

## ACKNOWLEDGEMENTS

The authors thank the Engineering and Physical Science Research Council for the computational time made available

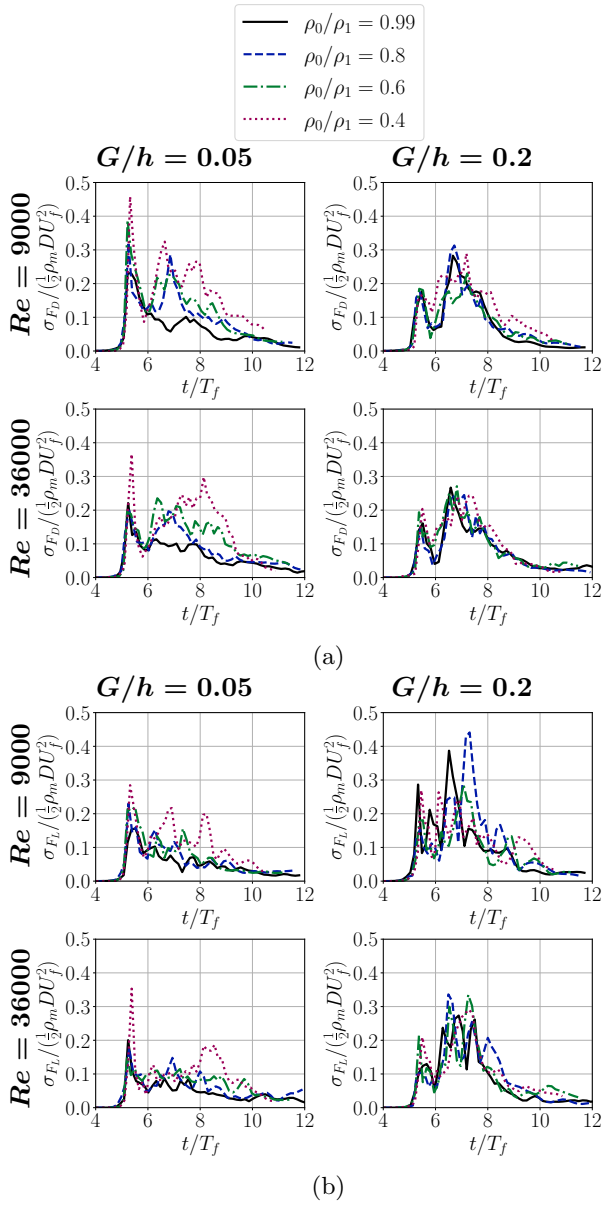


Figure 7. Standard deviation of the force components in the spanwise direction.

on the UK supercomputing ARCHER2 facility via the UK Turbulence Consortium (EP/R029326/1). For the purpose of open access, the first author has applied a Creative Commons Attribution (CC BY) licence to any Author Accepted Manuscript version arising from this submission.

## REFERENCES

- Albert, D. 2014 Non-Boussinesq gravity currents propagating on different bottom slopes. *J. Fluid Mech.* **741**, 658–680.
- Bartholomew, P., Deskos, G., Frantz, R. A. S., Schuch, F. N., Lamballais, E. & Laizet, S. 2020 Xcompact3D: An open-source framework for solving turbulence problems on a Cartesian mesh. *SoftwareX* **12** (100550).
- Bartholomew, P. & Laizet, S. 2019 A new highly scalable, high-order accurate framework for variable-density flows: Application to non-Boussinesq gravity currents. *Comput. Phys. Commun.* **242**, 83–94.
- Birman, VK, Martin, JE & Meiburg, E 2005 The non-boussinesq lock-exchange problem. part 2. high-resolution simulations. *J. Fluid Mech.* **537**, 125–144.
- Brito, M., Ferreira, R. M. L., Sousa, A., Farias, R., Lollo, G. Di, Ricardo, A. M. & Gil, L. 2022 LES validation of lock-exchange density currents interacting with an emergent bluff obstacle. *Environ. Fluid Mech.* **22**, 1055–1079.
- Ermanyuk, E. V. & Gavrilov, N. V. 2005a Interaction of an internal gravity current with a submerged circular cylinder. *J. Appl. Mech. Tech. Phys.* **46** (2), 216–223.
- Ermanyuk, E. V. & Gavrilov, N. V. 2005b Interaction of Internal Gravity Current with an Obstacle on the Channel Bottom. *J. Appl. Mech. Tech. Phys.* **46** (4), 489–495.
- Espath, LFR, Pinto, LC, Laizet, S & Silvestrini, JH 2015 High-fidelity simulations of the lobe-and-cleft structures and the deposition map in particle-driven gravity currents. *Phys. Fluids* **27** (5).
- Espath, LFR, Pinto, LC, Laizet, Sylvain & Silvestrini, Jorge Hugo 2014 Two- and three-dimensional direct numerical simulation of particle-laden gravity currents. *Comput. Geosci.* **63**, 9–16.
- Frantz, Ricardo AS, Deskos, Georgios, Laizet, Sylvain & Silvestrini, Jorge H 2021 High-fidelity simulations of gravity currents using a high-order finite-difference spectral vanishing viscosity approach. *Comput. Fluids* **221**, 104902.
- Gonzalez-Juez, E. & Meiburg, E. 2009 Shallow-water analysis of gravity-current flows past isolated obstacles. *J. Fluid Mech.* **635**, 415–438.
- Gonzalez-Juez, E., Meiburg, E. & Constantinescu, G. 2009 Gravity currents impinging on bottom-mounted square cylinders: flow fields and associated forces. *J. Fluid Mech.* **631**, 65–102.
- Gonzalez-Juez, E., Meiburg, E., Tokyay, T. & Constantinescu, G. 2010 Gravity current flow past a circular cylinder: forces, wall shear stresses and implications for scour. *J. Fluid Mech.* **649**, 69–102.
- Haugen, Nils Erland L & Brandenburg, Axel 2004 Inertial range scaling in numerical turbulence with hyperviscosity. *Phys. Rev. E* **70** (2), 026405.
- Laizet, S. & Lamballais, E. 2009 High-order compact schemes for incompressible flows: A simple and efficient method with quasi-spectral accuracy. *J. Comput. Phys.* **228** (16), 5989–6015.
- Maggi, M. R., Adduce, C. & Lane-Serff, G. F. 2023 Gravity currents interacting with slopes and overhangs. *Adv. Water Resour.* **171** (104339).
- Ozan, A. Y., Constantinescu, G. & Hogg, A. J. 2015 Lock-exchange gravity currents propagating in a channel containing an array of obstacles. *J. Fluid Mech.* **765**, 544–575.
- Shin, JO, Dalziel, SB & Linden, PF 2004 Gravity currents produced by lock exchange. *J. Fluid Mech.* **521**, 1–34.
- Tokyay, T. & Constantinescu, G. 2015 The effects of a submerged non-erodible triangular obstacle on bottom propagating gravity currents. *Phys. Fluids* **27** (5), 056601.
- Wang, J. H. & Yoon, H. S. 2015 Large eddy simulation of gravity current flow past a circular cylinder using immersed boundary method. In *Proc. ASME-JSME-KSME 2015 Joint Fluids Eng. Conf.*, pp. 1–6. Seoul, South Korea.
- Xie, P., Du, Y. & Chu, V. H. 2022 Impact forces by a gravity current on a circular cylinder above the seabed. *Appl. Ocean Res.* **125** (103243).
- Zhou, J. & Venayagamoorthy, S. K. 2017 Numerical simulations of intrusive gravity currents interacting with a bottom-mounted obstacle in a continuously stratified ambient. *Environ. Fluid Mech.* **17** (2), 191–209.